

System Design and Control of a Resonant Fast Steering Mirror for Lissajous-based Scanning

Ernst Csencsics, and Georg Schitter, *Senior Member, IEEE*

Abstract—This work introduces a system and controller design of an electromagnetically actuated fast steering mirror (FSM) tailored for Lissajous trajectories. The proposed system enables an improved performance in terms of energy consumption and tracking precision. By individually tuning the stiffness of each scan axis of the proposed FSM system, the resonance frequencies are placed at the drive frequencies of the desired Lissajous trajectory. The design of a dual tone controller for feedback control is presented, matched to the scanning trajectory and the tuned FSM dynamics. It is shown that compared to a state of the art FSM system the energy consumption can be reduced by a factor of 100 using the modified system structure and the dual tone controller. Vice-versa the maximum scan area is enlarged by a factor of 60. The resulting rms tracking error can be reduced by 48% as compared to the conventional FSM system.

Index Terms—System analysis and design, Optimal control, Motion control, Lissajous trajectory, Fast steering mirror

I. INTRODUCTION

Fast steering mirrors (FSMs) are applied for beam stabilization in optical systems [1], acquisition of optical signals and tracking of objects [2], and pointing of a laser or light beam [3]. Next to pointing applications FSMs are used for scanning operations ranging from optical free space communication [4], over laser scanners [5] to scanning confocal microscopy [6], scanning optical lithography [7] and material processing [8]. Depending on the application requirements, such as scan range and system bandwidth, electromagnetically [1], [5] and piezoelectrically [4], [9] actuated systems are reported. FSMs are typically operated in closed-loop with high bandwidth feedback controllers for fast motion control and disturbance rejection [10], [11].

For 2-dimensional scanning of an area of interest a laser beam is deflected by tilting the FSM around two rotational axes. Raster scan trajectories are commonly employed patterns [8], [12] and are also applied in in other scanning systems, e.g. in scanning probe microscopy (SPM) [13]. The FSM system axes are driven with a slow and a fast triangular signal, resulting in a uniform spatial resolution and scan speed. For a triangular reference signal at least the first 7 harmonics of the fundamental frequency have to be covered by the system bandwidth [14]. This requires a high control bandwidth [15] to achieve high spatial resolution at high frame rates. Simultaneously this imposes strong requirements on the mechanical design of the FSM [16], since structural modes

within the targeted system bandwidth have to be avoided [17].

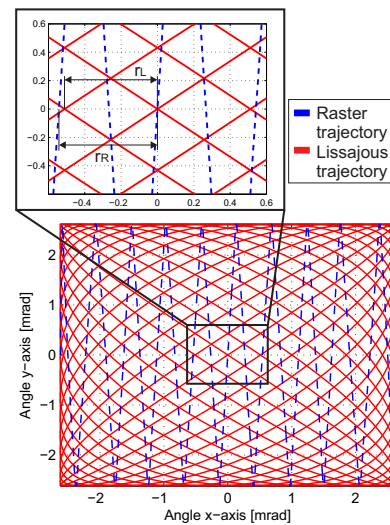


Fig. 1. Lissajous trajectory (solid red) compared to raster trajectory (dashed blue) for a FSM system with a scan size of 5.24×5.24 mrad (10% of the used FSM system range) and a framerate of 1 frame/s. The fast scanning axis of the raster scan is set to 10 Hz and the Lissajous frequencies are $f_x=19$ Hz and $f_y=14$ Hz, resulting in an almost equal spatial resolution for the raster (r_R) and for the Lissajous (r_L) scan (zoomed image).

Recently Lissajous-based scan trajectories have been proposed for precision scanning systems such as atomic force microscopes (AFMs) [18]. They result from driving each system axis with a sinusoidal signal of a single frequency, with the drive frequencies determining the spatial resolution and the frame rate [19]. The scanning speed is not constant and adjacent areas are traversed from different directions, which can be critical for tactile metrology systems (e.g. artifacts in AFMs) but not for optical systems. The spatial resolution is non-uniform, with the maximum distance between two intersections of the scan trajectory and the principle axes being an efficient metric for it (see Fig. 1). In Fig. 1 a comparison of a raster and a Lissajous scan trajectory with almost equal resolution and frame rate is shown. Together with a tailored feedback controller they are reported to enable a reduction of the sensor noise feedback in high precision scanning applications [18]. They have been applied in various scientific fields like optical microscopy [20] or medical imaging [21]. Their multi-resolution capabilities in AFM applications have been

The authors are with the Christian Doppler Laboratory for Precision Engineering for Automated In-Line Metrology at the Automation and Control Institute, Technische Universität Wien, A-1040 Vienna, Austria. Corresponding author email: csencsics@acin.tuwien.ac.at.

demonstrated [18] and they have been applied in video-rate AFM [22]. Further applications include also magnetic particle imaging [23] and MEMS scanners [24].

Recently Lissajous trajectories have been applied to a FSM system for improving the system performance [25]. Compared to a raster trajectory with equal spatial resolution and frame rate, the Lissajous trajectory in combination with a dual tone (DT) controller enables significantly improved tracking performance. For a scan with equal scan amplitude, however, the Lissajous trajectory required more than twice the actuation current, limiting the achievable bandwidth and scan range.

This paper proposes a method to improve the energy efficiency and to enlarge the achievable scan range of a state of the art FSM system by modifying the resonance frequencies of the system axes in order to match the drive frequencies of the desired Lissajous scanning trajectory. Tuning the resonances has recently also been reported for a micromirror system to adjust the scanning direction and frequency [26].

A system analysis of the conventional commercial FSM is performed in Section II, describing the experimental setup and identifying the structural modes that limit the system bandwidth. In Section III the modifications on the tuned FSM system are described, the system dynamics are identified and compared to the conventional FSM system. Section IV presents the Lissajous trajectory tailored controller design for both FSM systems. DT controllers [25] are designed for the conventional and the tuned FSM, respectively. To improve the tracking performance a two degree of freedom control structure is introduced. The performance of both systems with the respective controllers is evaluated in Section V, while Section VI concludes the paper.

II. CONVENTIONAL FSM SYSTEM

A. System description

A state of the art commercial FSM (Type: OIM101, Optics in Motion LLC, Long Beach, USA) with a maximum range of ± 26.2 mrad (± 1.5 deg) is used as benchmark system. To actuate each axis two voice coil actuators with moving magnets and static coils, operated in a push-pull configuration, are used. To measure the rotational position of the mirror around x- and y-axis for closed-loop operation, an internal optical sensor system with read-out electronics is used. Each pair of actuator coils is driven by a custom made current amplifier (OPA544T, Texas Instruments Inc., Dallas, TX, USA) with a bandwidth of 10 kHz. The signals for the amplifier inputs (x_{in} and y_{in}) are generated by a dSpace platform (Type: DS1202, dSPACE GmbH, Germany), that is also used for data acquisition of the sensor signals (x_{out} and y_{out}). As the actuation and sensing axes of the FSM are 45° rotated with respect to each other, the dSpace system is also used to implement a rotation matrix for transforming the drive signals. Fig. 2 shows a schematic of the resulting system setup, with the digital system, the FSM, the two current amplifiers (I_x and I_y) and the internal position sensor PS (Θ_x and Θ_y). The transfer functions of the axes are denoted by G_{xx} and G_{yy} , while G_{xy} and G_{yx} represent the crosstalk in the system.

To identify potential structural modes of the mover with the mirror an external capacitive sensor CS (Type: 6504,

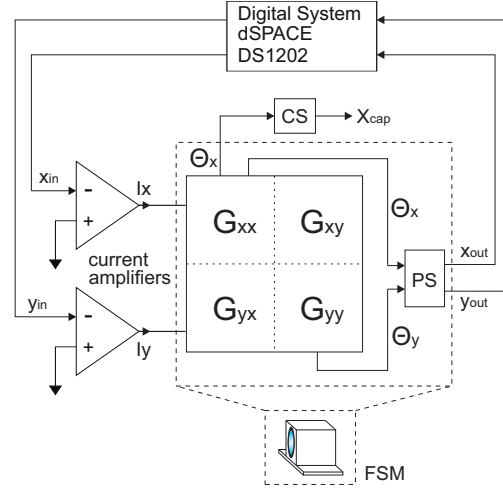


Fig. 2. Schematic of the experimental FSM setup. The actuators of the x- and y-axis are driven by the currents I_x and I_y with current controlled amplifiers. The transfer functions of both axes are denoted by G_{xx} and G_{yy} . The crosstalk between the axes is represented by the grey blocks G_{xy} and G_{yx} . The mirror angles Θ_x and Θ_y are measured with an internal optical position sensor PS .

MicroSense LLC, Lowell, MA, USA) is additionally used to identify the x-axis dynamics. The sensor is mounted in front of the mover and collocated above the center of one voice coil actuator (see Fig. 4) to measure the rotational position of the mover around the x-axis (x_{cap} in Fig. 2).

B. System identification and modeling

A system analyzer (3562A, Hewlett-Packard, Palo Alto, CA, USA) is used for system identification. The input of the current amplifier and the signal of the internal sensor are considered as the system input and output, respectively (see Fig. 2). Thus the amplifier, the mirror and the internal sensor are together considered as the plant. Fig. 3a depicts the measured frequency response of the x-axis, as well as the magnitude plot of the measured crosstalk from x- to y-axis. As shown in [25] the frequency responses of both axes are identical for this system, due to the symmetric design, which also holds for the crosstalk frequency responses. The crosstalk magnitude between the axes at the resonance frequency is 38 dB lower than the magnitude of the single axis transfer functions (TFs). At DC and over the most part of the relevant frequency spectrum the crosstalk is more than 44 dB lower than the single axis TFs. This justifies the use of one SISO controller per system axis.

The second order plant model

$$G_{xx}(s) = G_{yy}(s) = K \cdot \frac{\omega_0^2}{s^2 + 2\omega_0\zeta s + \omega_0^2} \cdot P_A(s), \quad (1)$$

with a DC gain $K=11.22$, $\omega_0=169.6$ rad/s (suspension mode at $f_0=27$ Hz) and a damping ratio $\zeta=0.04$ is fitted to the measured data of the system axes. The phase loss due to the sampling of the digital system at $T_s=20\mu s$, is modeled by a second order Pade-approximation $P_A(s)$ [27] for the controller design.

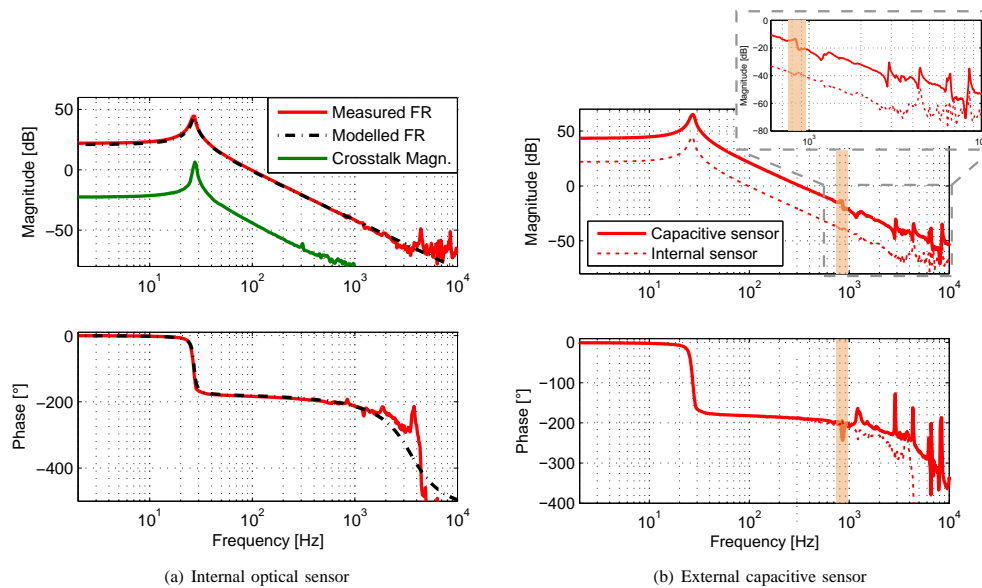


Fig. 3. Frequency responses of the conventional FSM. (a) shows the measurement with the internal sensor system (solid red) and the fitted system model (dashed black) for a single scan axis. The system is modeled as a mass-spring-damper system with a resonance frequency $f_0=27$ Hz. Structural modes occur beyond 4 kHz. The measured crosstalk between the two axes (solid green) is about 40 dB below the single axis response. (b) depicts the frequency response measured with the external capacitive sensor (co-located with actuator), showing the same low frequency behavior. Additionally structural modes at 850 Hz (marked area in zoomed image) and beyond 2.8 kHz are observed.

Fig. 3b shows the frequency response measured with the capacitive sensor (solid) and compares it to the measurement using the internal sensor (dotted). The vertical shift of the magnitude plots and the different time delays in the phase plot (visible beyond 1 kHz) result from the different gains and sampling times of the two sensor systems. The measurement using the capacitive sensor reveals first structural modes of the mirror around 850 Hz (marked area in the zoomed image), which are not observable with the internal sensor. From the phase plot also a phase drop down to -242° around 850 Hz can be observed. Besides the structural modes at 4.4 kHz and 8.5 kHz, which are observable with both sensors, the capacitive sensor also shows additional structural modes at 2.9 kHz and 6.6 kHz. The additional modes result from deformations of the mover with mode shapes that have nodes at the measurement position of the internal sensor and can thus not be observed.

From a pure controls perspective the sensor placement of the internal sensors is a benefit rather than a drawback, since the unobservable mode at 850 Hz does not cause a phase drop and is thus not limiting the achievable closed-loop bandwidth of the PID controlled system. It would thus be possible to push the closed-loop bandwidth above 850 Hz using the internal sensors. However, for a precise scanning motion the first structural mode, denotes an upper limit for the maximum drive frequency of the mirror. The structural mode of the mirror may lead to deviations of the steered beam on the target, which cannot be compensated for.

With the identified system dynamics and a targeted scanning application with an image size of 300x300 pixel and a frame

rate of 1 frame/s a suitable Lissajous trajectory needs to be designed. For the choice of the two drive frequencies two competing thoughts need to be considered: (i) the frequencies need to be well separated in order to reduce the crosstalk in the tuned FSM system (see Section III-B) and (ii) the difference between the two frequencies should be small enough, such that the resolution along the two principal axes is not significantly different. According to these requirements the two drive frequencies should range between 700 Hz (approx. 10% lower than first structural mode) and 400 Hz. From this range the frequencies $f_1=473$ Hz and $f_2=632$ Hz are chosen. According to the definition in [18] they result in a spatial resolution of 0.0025 and 0.0033 (with respect to unity image size) for the two principal axes, clearly enabling a 300x300 pixel image, and a trajectory duration of $T=1$ s (1 frame/s).

III. TUNED FSM SYSTEM

To improve the energy efficiency for a Lissajous scan with the desired frequencies f_1 and f_2 a modified system design is employed. The conventional FSM is with f_1 and f_2 driven on its mass line (see Fig. 3). An improvement of energy efficiency of the system can be achieved by lifting the plant gain. This is realized by shifting the resonance frequencies of each axis in order to match one of the desired drive frequencies, resulting in an increased plant gain at these frequencies only. At resonance the force applied to the system is in phase with the velocity (direction of the movement), transferring energy from actuator force to mechanical movement with maximum efficiency. This approach is perfectly suitable for the Lissajous scan case,

where a high plant gain is only needed at the individual drive frequency.

A. System description

For the setup of the tuned FSM system the same components as for the conventional FSM (see Section II-B) are used. For a second order rotational mass-spring-damper system the resonance frequency of each axis is defined by

$$f_0 = \frac{1}{2\pi} \cdot \sqrt{\frac{k_r}{J}}, \quad (2)$$

where k_r is the rotational spring constant and J is the inertia of the moved body. Given the resonance frequency $f_0=27$ Hz of the conventional FSM and the targeted drive frequencies of $f_1=473$ Hz and $f_2=632$ Hz, the resonance frequencies of the axes need to be increased. The inertia of the moved body is given by the conventional FSM and equal for both axes. This leaves the rotational stiffness of each axis as parameter to individually tune the resonance frequencies to the desired values f_1 and f_2 . A leaf spring (brass, 20mm wide, 1mm thick) is attached to the mover for each axis and mounted to an external mounting frame. The respective stiffness is tuned by changing the length of the individual leaf spring via the position of the clamping bracket. In Fig. 4 the tuned FSM system setup is shown.

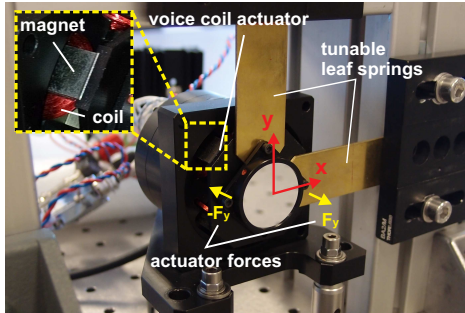


Fig. 4. Tuned FSM system. The spring constants of x- and y-axis are increased using tunable leaf springs. The leaf springs are attached to the mover part and are mounted to a solid aluminium frame. The resonance frequencies can be tuned by adjusting the length of the leaf springs, changing their stiffness.

B. Identification and modeling

Considering the input of the current amplifier and the signal of the internal sensor again as the system input and output, respectively, the system identification is performed with a system analyzer (see Section II). Fig. 5a shows the measured frequency responses of the tuned x- and y-axis. It can be seen that the resonance frequency of the x-axis is tuned to $f_{0x}=473$ Hz by increasing the system stiffness by a factor of about 512 as compared to the conventional FSM. The resonance frequency of the y-axis is tuned to $f_{0y}=632$ Hz, corresponding to a stiffness increase by a factor of 630. Around 2 kHz the system noise floor at about -60 dB is reached. Fig. 5a also depicts the magnitude response of

the crosstalk between both axes (equal for both directions), showing that the crosstalk magnitude at DC is 18 dB smaller than the one of the y-axis. This means that the crosstalk between the axes at DC is increased by 26 dB as compared to the conventional FSM. Tuning both axes to the same frequency, e.g. f_{0x} (which would make no sense for the trajectory), or only slightly diverging frequencies, would result in an approximated crosstalk magnitude around 12 dB below the axis TF at f_{0x} , when considering the difference of the axis and crosstalk response of the conventional FSM at resonance (38 dB, see Fig. 3a) and the reduced difference of axis and crosstalk response of the tuned FSM at DC (26 dB smaller). When separating the two resonance frequencies the resonances of both axes can no longer amplify each other via crosstalk, so that the resulting crosstalk peaks are reduced. Thus the crosstalk magnitudes at f_{0x} and f_{0y} stay below 20 dB and 26 dB, respectively. In summary this again justifies the use of one SISO controller per axis.

The second order plant models for the x- ($G_{xx,t}(s)$) and y-axis ($G_{yy,t}(s)$) are fitted to the measured data, using the same structure as in (1) and identified parameters as shown in Table I. As the digital system is not changed the phase loss due to its sampling delay is modeled by the same Pade-approximation as in (1).

TABLE I
PARAMETERS OF THE TUNED FSM SYSTEM MODELS.

Model	Parameter	Value
$G_{xx,t}(s)$	K	0.0219
	ω_0	2971 rad/s
	ζ	0.008
$G_{yy,t}(s)$	K	0.0178
	ω_0	3971 rad/s
	ζ	0.008

The plant models of the tuned FSM are depicted in Fig. 5b together with the plant model of the conventional FSM. It can be seen that compared to the conventional FSM the spring line is shifted by 54.2 dB and 56 dB for the x- and y-axis, respectively, resulting in a stiffer system with higher resonance frequencies. At the targeted drive frequencies the plant gain of the tuned FSM is 31.6 dB (x-axis) and 34.6 dB (y-axis) larger than the plant gain of the conventional FSM. This already implies that at these frequencies the controller for the tuned FSM will require less effort, denoting less actuator current, to result in the same targeted loop gain. The slightly varying mass lines of the tuned FSM axes result from additional inertia due to the mounted leaf springs. Clearly the material choice of the leaf springs is an important parameter as mainly the material-inherent damping limits the quality factor Q of the resonances, and thus the increase in energy efficiency.

IV. CONTROLLER DESIGN FOR LISSAJOUS BASED SCANNING

In contrast to tracking raster trajectories for each scanning direction, the controller for a Lissajous trajectory needs to

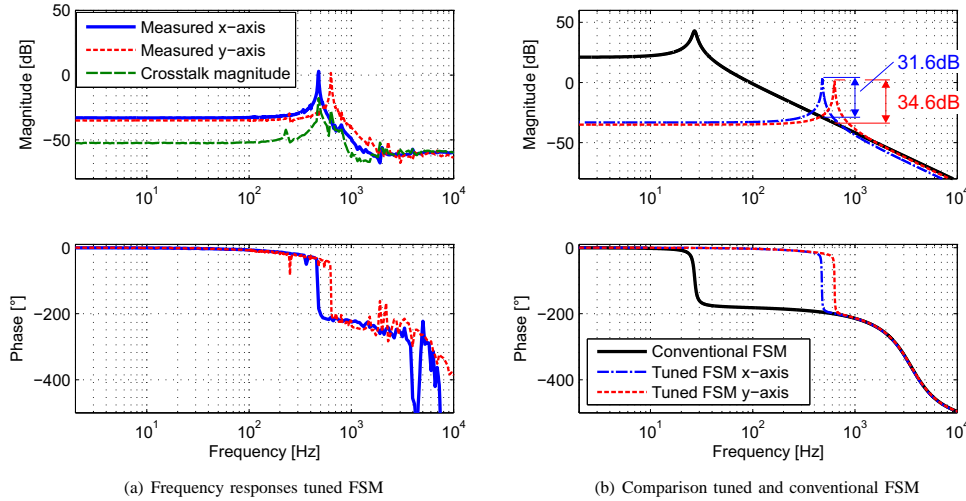


Fig. 5. Frequency responses of the tuned FSM. (a) shows the frequency response of the x- (blue) and y-axis (red) of the tuned FSM. The resonance frequencies of both axes are shifted to $f_{0x}=473$ Hz (x-axis) and $f_{0y}=632$ Hz (y-axis). The crosstalk magnitude (green) is about 20 dB below the single axis responses. (b) compares the fitted system axis models of the conventional (solid black) and tuned FSM dynamics (dash-dotted blue and red). The stiffness of the system is increased by more than 54 dB. At the drive frequencies the plant gain of the tuned FSM is increased by more than 30 dB.

track a single frequency only. Tailored DT controllers are reported [25] to be suitable for Lissajous-based scanning of low-stiffness FSMs. They are simultaneously tracking a sinusoidal signal at the drive frequency of the individual axis and rejecting the crosstalk with the drive frequency from the respectively second scanning axis.

A. Dual tone controller design methodology

To design DT controllers for the axes of the conventional and the tuned FSM an H_∞ approach [28] is used. The controller for a single system axis is obtained by minimizing the H_∞ -norm

$$\min_C \left\| \begin{bmatrix} W_S S \\ W_U U \end{bmatrix} \right\|_\infty = \|N\|_\infty < \gamma. \quad (3)$$

of the extended system model shown in Fig. 6. P represents the plant dynamics, C the controller, and W_S and W_U are the weighting functions for the sensitivity function $S(s) = 1/[1 + C(s)P(s)]$ and the input sensitivity function $U(s) = P(s)/[1 + C(s)P(s)]$, respectively, that guide the controller design. An upper bound for the H_∞ -norm is represented by γ , where $\gamma < 1$ should be maintained to ensure robust stability. In Fig. 6 p denotes the sensed mirror position, u is the control effort, e the tracking error, r the reference, and n is the sensor noise.

As in [25] the weighting function W_S , representing the requirements on S , is composed of a fourth order TF

$$W_S(s) = \prod_{i=1}^2 \frac{s^2 + 2\omega_{ri}\zeta_i s + \omega_{ri}^2}{s^2 + 2\omega_{ri}\zeta_i s + \omega_{ri}^2}. \quad (4)$$

This TF consists of two inverse notch filters with peaks at the two drive frequencies and steep roll-offs before and

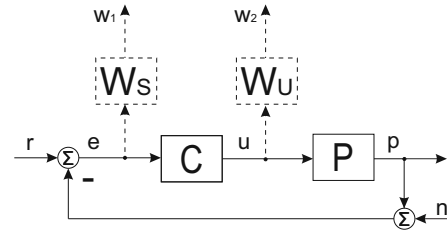


Fig. 6. Block diagram of the extended model of the H_∞ -controller design for a single FSM axis. The weighting functions for the sensitivity and input sensitivity function are represented by W_S and W_U . C denotes the controller and P the FSM axis plant model.

thereafter, enforcing good tracking at these two frequencies only. The peak frequencies are set to $\omega_{r1}=2971$ rad/s (f_1) and $\omega_{r2}=3971$ rad/s (f_2) matching the two drive frequencies, that coincide with the resonances of the two scanning axes. The damping ratio $\zeta=0.01$ and the factor $d=100$ are used to tune the width and height of the inverse notches.

To enforce a reduced control effort at high and low frequencies the weighting function

$$W_U(s) = K \cdot \prod_{i=1}^2 \frac{s^2 + 2\zeta_{zi}\omega_{zi} + \omega_{zi}^2}{s^2 + 2\zeta_{pi}\omega_{pi} + \omega_{pi}^2}, \quad (5)$$

with gain $K=2.886 \times 10^5$ and parameters according to Table II, is used to formulate the requirements on U . The weighting function is composed of an inverse highpass and an inverse lowpass filter and reaches its minimum between 400 Hz and 700 Hz. This ensures a second order roll-on and roll-off of the controller at low and high frequencies, respectively, enforcing

TABLE II
PARAMETERS OF THE WEIGHTING FUNCTION W_U .

Index	ω_{Index} [rad/s]	ζ_{Index}
z_1	3.77×10^3	0.7
z_2	4.4×10^3	0.7
p_1	3.77×10^7	0.7
p_2	0.063	0.7

a reduced control effort. Around the drive frequencies, however, the constraints on the control effort are relaxed, such that good tracking in this frequency range is not impaired by a limited controller output.

B. DT controller for conventional FSM

With the obtained system model from Section II-B and the design methodology from the previous Section the controller C_{DT} for the conventional FSM is of 9th order:

$$C_{DT}(s) = K_{DT} \cdot \frac{\left(\prod_{i=1}^3 s^2 + 2\zeta_{z_i} \omega_{z_i} s + \omega_{z_i}^2 \right) \cdot (s + \omega_{z_4})}{\left(\prod_{i=1}^4 s^2 + 2\zeta_{p_i} \omega_{p_i} s + \omega_{p_i}^2 \right) \cdot (s + \omega_{p_5})}, \quad (6)$$

with gain $K_{DT}=7.285 \times 10^8$ and coefficients according to Table III. The magnitude response of the designed controller is

TABLE III
COEFFICIENTS OF THE DUAL TONE CONTROLLER $C_{DT}(s)$ FOR THE CONVENTIONAL FSM.

Index	ω_{Index} [rad/s]	ζ_{Index}
z_1	0.024	0.97
z_2	169	4×10^{-2}
z_3	-3340	2.5×10^{-2}
z_4	-4310	-
p_1	76.8	0.93
p_2	2.79×10^3	1×10^{-4}
p_3	3.79×10^3	1×10^{-4}
p_4	1.12×10^4	0.4
p_5	1.68×10^4	-

shown in Fig. 7. The controller shows high control gains of 70 dB and 77 dB at the drive frequencies $f_1=473$ Hz and $f_2=632$ Hz, respectively. At frequencies below 300 Hz the controller shows a 40 dB/dec slope with a pair of conjugate complex zeros at the resonance frequency of the plant at $f_0=27$ Hz. This pair of zeros is used to reduce the high loop gain at the system resonance, which is not required at this frequency, and would lead to increased sensor noise feedback. The 40 dB/dec slope below 27 Hz is caused by the weighting function W_U and reduces the loop gain at small frequencies, while the 40 dB/dec slope between 27 Hz and 300 Hz is caused by the system dynamics. Above 2 kHz the controller shows a -40 dB/dec slope, which results from the weighting function

W_U and reduces loop gain at high frequencies. As the high controller gains lie on the mass line of the conventional FSM, the control system is robust against even significant parameter variations (e.g. mass or stiffness).

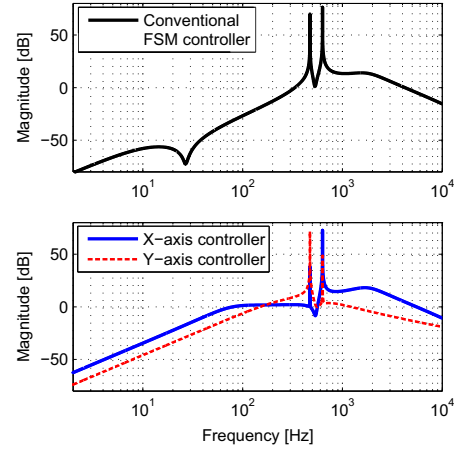


Fig. 7. Magnitude responses of the designed controllers C_{DT} (black), and C_x (blue) and C_y (red) for the conventional and the tuned FSM, respectively. C_{DT} shows highly localized control efforts at the drive frequencies $f_1=473$ Hz and $f_2=632$ Hz. The different values result from different plant gains at these frequencies. C_x and C_y show the largest gain at the drive frequency of the respectively other axis (reject crosstalk) and smaller gains at their own drive frequency (tracking). At low and high frequencies C_{DT} and C_x show a second order roll-on and roll-off, respectively. C_y shows a second order roll-on at low and a first order roll-off at high frequencies.

The system is built symmetrically and the controller is tuned for both drive frequencies, so that the same controller can be applied for both system axes.

C. DT controller for tuned FSM

The DT controllers for the tuned FSM system are also designed by using the design procedure and weighting functions described in Section IV-A. Given the system model for the x-axis of the tuned FSM system, obtained in Section III-B, the derived controller is:

$$C_x(s) = \frac{K_x}{K_{DT}} \cdot C_{DT}(s), \quad (7)$$

with $C_{DT}(s)$ from (6), gain $K_x=1.251 \times 10^9$ and coefficients according to Table IV. The H_∞ -design is done in the continuous time domain, so that poles and zeros above the sampling frequency are removed before discretization, resulting in a reduced 9th order controller.

Using the system model of the y-axis from Section III-B in the controller design procedure, the derived reduced controller

for the y-axis is of 8th order:

$$C_y(s) = K_y \cdot \frac{\left(\prod_{i=1}^2 s^2 + 2\zeta_{z_i}\omega_{z_i}s + \omega_{z_i}^2 \right) \cdot \left(\prod_{i=3}^5 s + \omega_{z_i} \right)}{\prod_{i=1}^4 s^2 + 2\zeta_{p_i}\omega_{p_i}s + \omega_{p_i}^2}, \quad (8)$$

with gain $K_y=6.616 \times 10^3$ and coefficients according to Table IV.

TABLE IV
COEFFICIENTS OF THE CONTROLLERS $C_x(s)$ AND $C_y(s)$ FOR THE X- AND Y-AXIS OF THE TUNED FSM.

Index	$C_x(s)$		$C_y(s)$	
	ω_{Index} [rad/s]	ζ_{Index}	ω_{Index} [rad/s]	ζ_{Index}
z_1	-0.063	1.9×10^{-3}	-3.43×10^3	6×10^{-2}
z_2	2.97×10^3	8×10^{-3}	3.97×10^3	2×10^{-2}
z_3	-3.38×10^3	2.7×10^{-2}	0.044	-
z_4	-2.55×10^3	-	0.059	-
z_5	-	-	-4.47×10^3	-
p_1	485	0.53	1.37×10^3	0.79
p_2	2.97×10^3	9.5×10^{-5}	2.97×10^3	1×10^{-4}
p_3	3.97×10^3	9.5×10^{-5}	3.97×10^3	1×10^{-4}
p_4	1.13×10^4	0.37	4.04×10^3	0.57
p_5	1.65×10^4	-	-	-

The magnitude responses of the designed controllers for x- and y-axis are shown in Fig. 7. It can be seen that again both controllers show highly localized control efforts at the drive frequencies, due to W_S . However, the control effort at the designated drive frequency of each axis is significantly reduced, in comparison to the conventional FSM plant controllers (see Table V). This results from the higher plant gain at the respective resonance frequency. At the respective crosstalk frequency (drive frequency of the other axis) the control effort is equal or slightly reduced. Both controllers show low control efforts and a 40 dB/dec roll-on at low frequencies, due to W_U . At high frequencies C_x and C_y show a -40 dB/dec and -20 dB/dec roll-off (to fulfill the requirements on $U(s)$), respectively, while the gain of C_y lies constantly below the gain of C_x . The deviations of the controller TFs at low and high frequencies result from the optimization process that uses the same weighting functions but different plant models and aims to fulfill the phase requirements in both cases.

TABLE V
CONTROLLER GAINS OF $C_{DT}(s)$, $C_x(s)$ AND $C_y(s)$ AT THE DRIVE FREQUENCIES.

Frequency [Hz]	C_{DT} [dB]	C_x [dB]	C_y [dB]
$f_1 = f_{0x} = 473$	70	38	70
$f_2 = f_{0y} = 632$	77	73	48

D. Controller implementation

For implementation on the dSpace system the controllers are discretized using Pole-Zero-Matching [29] for a sampling frequency of $f_s=50$ kHz. Using the relation $z = e^{s/f_s}$, poles and zeros are directly transformed to the discrete time domain, ensuring that the controller poles are located exactly at the drive frequencies.

The simulated open loop frequency responses of both systems are shown in Fig. 8a. At low frequencies the TFs of the tuned FSM are dominated by the controller, while the TF of the conventional FSM is flat due to the cancellation of the plant dynamics by the controller between f_0 and f_1 . The gains at the two drive frequencies lie for both systems around 48 dB. The roll-off above the drive frequencies is a combination of the controller roll-off and the low-pass characteristic of the systems. Considering parameter variations, the control system is robust against changes of the axis resonance frequencies up to 15%. The more critical change is when the resonance frequencies of the axes approach each other, while a change that increases the gap between the resonance frequencies is less critical (robust to changes up to 50%). Robustness of the system thus also supports the desire for well separated drive frequencies (see Section III-B).

The measured complementary sensitivity functions of the feedback controlled conventional and tuned FSM are depicted in Fig. 8b. It shows that the TFs of both systems reach the 0 dB line exactly at the two drive frequencies f_1 and f_2 and roll-on/off steeply before/after. At these frequencies the TFs show perfect phase match of 360° and 720° , which is achieved by two right half plane zeros. This phase match is achieved at the cost of a positioning delay of 1 and 2 periods, respectively, which, however, can easily be accounted for by post-preprocessing of the acquired data. Below the resonance frequency f_0 of the plant the TF shows a 40 dB/dec slope resulting from the controller TF. Above 2 kHz a -80 dB/dec slope can be obtained. The TF of the tuned FSM both show a 40 dB/dec roll-on at low frequencies while at high frequencies the x-axis and the y-axis show a -80 dB/dec and -60 dB/dec roll-off, respectively. The differences in the closed-loop TFs at low and high frequencies result from the differences in the controllers that are due to the H_∞ -design (see Section IV-C).

V. EXPERIMENTAL RESULTS

To investigate the closed-loop system performance both systems are tracking the desired reference Lissajous trajectory with different scan amplitudes. The scan amplitudes of both systems are increased until the current limit of the actuator coils is reached. The internal optical sensor is used for position measurement. The spatial tracking error is calculated as the rms value of the two dimensional euclidean distances between reference trajectory and measured position at every sampling point. For evaluation of the current consumption the sum rms current through the coils of both system axes, necessary to track the Lissajous pattern with the given scan amplitude, is measured.

Fig. 9a shows a comparison of the spatial rms tracking errors of the two system configurations for different scan amplitudes.

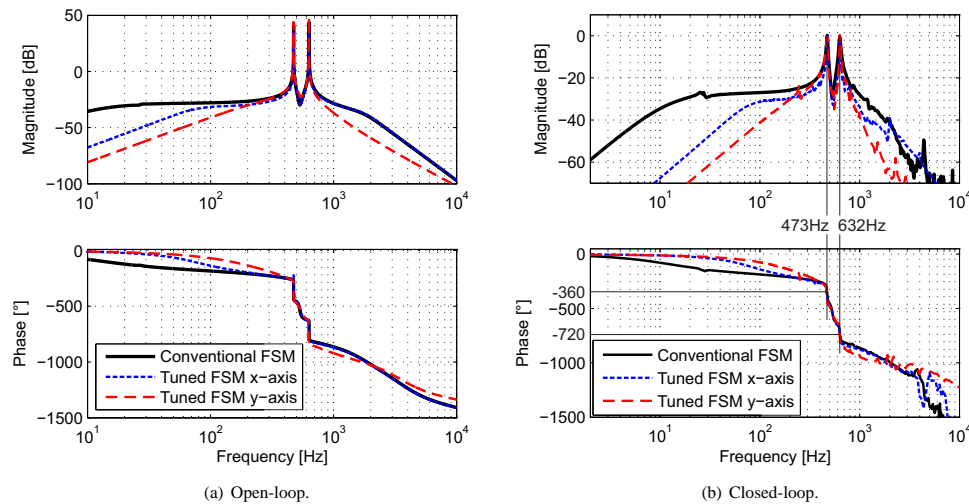


Fig. 8. Transfer functions of the conventional (black) and tuned FSM (x-axis blue, y-axis red) system. (a) shows the simulated open loop frequency responses of both systems. At low and high frequencies roll-ons and roll-offs due to the controller and plant dynamics are observable. At the drive frequencies (473/632 Hz) both systems show localized high loop gains around 48 dB. (b) depicts the measured complementary sensitivity functions of both system with the related controllers in closed-loop. At the drive frequencies the TFs of both systems reach 0 dB and the phase equals -360° and -720° , respectively.

The conventional FSM (black slope) shows a tracking error around 1.8% of the scan amplitude in the feasible scan range. The tuned FSM (red slope) shows a rms error below 1% for amplitudes smaller than 2 mrad and a slowly increasing error for larger amplitudes. This means that the resulting tracking error of the tuned FSM is 48% lower, as compared to the conventional FSM. With increasing amplitudes the rms error of the tuned FSM slightly increases and is 1.2% at the maximum scan amplitude of 2.62 mrad.

Fig. 9b depicts the current consumption of the conventional and the tuned FSM with DT controller for different drive amplitudes. The conventional FSM has a sum current consumption of 1.21 A at the smallest measured scan amplitude of 0.16 mrad and 2.61 A at the largest feasible scan amplitude of 0.34 mrad. The tuned FSM requires only a sum current of 0.12 A for a trajectory with a scan amplitude of 0.16 mrad. This current consumption is a factor 10 smaller, as compared to the conventional FSM, denoting a reduction of dissipated energy by a factor of 100. Due to the reduced current consumption the tuned FSM can reach a scan amplitude of 2.62 mrad (10% of the full amplitude range) before reaching the coil current limit, while the conventional FSM reaches only 0.34 mrad (1.6% of the full range amplitude). This means that the tuned FSM has a maximum scan amplitude which is 7.7 times larger than the one of the conventional FSM, equaling an about 60 times larger scan area.

To demonstrate the improvements of the tuned FSM a simple projection system consisting of the closed-loop controlled conventional/tuned FSM a modulated laser and a projection screen is set up. The FSM systems track the desired Lissajous trajectory with the related maximum scan amplitude and the synchronized laser is switched on/off to project the applied

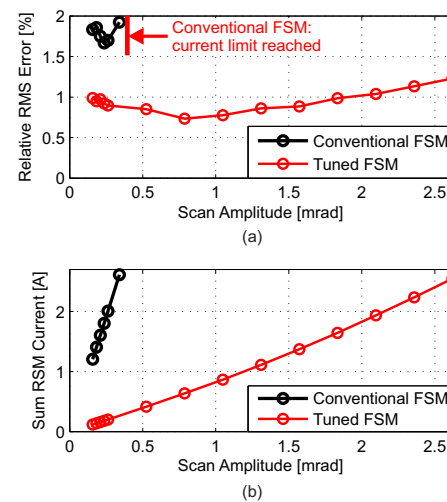


Fig. 9. Performance comparison of the conventional (black) and tuned FSM system (red) for different drive amplitudes. (a) compares the rms tracking error, which lies around 1.8% for the conventional FSM and feasible amplitudes. The error of the tuned FSM is 48% smaller. At the maximum scan amplitude the rms error of the tuned FSM is 1.2%. (b) compares the rms drive currents. The conventional FSM has a higher current consumption, reaching the current limit at a scan amplitude of 0.34 mrad. The current consumption of the tuned FSM is a factor 10 smaller at a scan amplitude of 0.16 mrad. The maximum amplitude of the tuned FSM before reaching the current limit is with 2.62 mrad a factor 7.7 larger than in the case of the conventional FSM.

pattern (TU Wien logo) on the 3m distant screen. The projected patterns are acquired with a conventional camera at shutter times of 0.1, 0.5 and 1 s, equaling 10%, 50% and 100% of the frame time, respectively (trajectory duration 1 s). Fig. 10 depicts the projected patterns, illustrating the significantly enlarged scan area. It also shows the gradually increasing resolution (multi-resolution property [18]) of a Lissajous scan with evolving scan time.

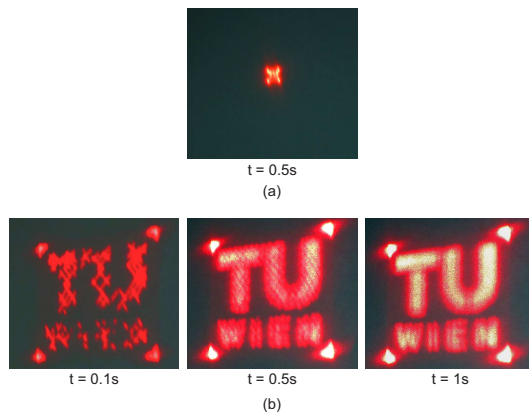


Fig. 10. Projection application using the conventional and the tuned FSM system. (a) shows the projection using the conventional FSM at maximum scan amplitude (0.34 mrad) and a shutter time of 0.5 s. (b) depicts the projection using the tuned FSM at maximum scan amplitude (2.62 mrad) and shutter times of 0.1, 0.5 and 1 s.

In summary, the design choice of placing the system's resonance frequencies at the drive frequencies of the desired Lissajous trajectory and applying the designed dual tone controllers reduces the current consumption by a factor of 10, enlarges the scan range by a factor of 7.7 and reduces the tracking error as compared to the conventional FSM system with DT controllers.

VI. CONCLUSION

In this paper an energy efficient design of a FSM system tailored for Lissajous-based scanning is proposed and a suited controller design is presented. To improve the energy efficiency as compared to a conventional FSM, the rotational stiffness of the FSM axes is modified, such that the resonance frequency of each axis matches the desired drive frequency. Tailored feedback dual tone controllers with highly localized control efforts at both drive frequencies are designed for tracking the Lissajous trajectory and crosstalk rejection. Due to the matched resonances, these controllers require less control effort at the individual drive frequency to reach the same loop gain as compared to controllers for a conventional FSM. Applying the dual tone controllers to the tuned FSM, the current consumption can be reduced by a factor of 10 as compared to a conventional FSM. Vice-versa the scan range of the tuned FSM is increased by a factor of 7.7. This represents a significant performance improvement of FSM systems for high resolution Lissajous-based scanning and makes them attractive

for future applications in optical scanning application, such as optical metrology systems. Current work is focused on the employment of phase-locked-loops to further increase the scanning precision.

ACKNOWLEDGMENT

The financial support by the Austrian Federal Ministry of Science, Research and Economy and the National Foundation for Research, Technology and Development, as well as MICRO-EPSILON MESSTECHNIK GmbH & Co. KG and ATENSOR Engineering and Technology Systems GmbH is gratefully acknowledged.

REFERENCES

- [1] D. J. Kluk, M. T. Boulet, and D. L. Trumper, "A high-bandwidth, high-precision, two-axis steering mirror with moving iron actuator," *Mechatronics*, vol. 22, no. 3, pp. 257–270, Apr 2012.
- [2] M. Guelman, A. Kogan, A. Livne, M. Orenstein, and H. Michalik, "Acquisition and pointing control for inter-satellite laser communications," *IEEE Transactions on Aerospace and Electronic Systems*, vol. 40, no. 4, p. 1239, 2004.
- [3] S. Xiang, P. Wang, S. Chen, X. Wu, D. Xiao, and X. Zheng, "The research of a novel single mirror 2d laser scanner," *Proc. of SPIE*, vol. 7382, Aug 2009.
- [4] H. F. Mokbel, W. Yuan, L. Q. Ying, C. G. Hua, and A. A. Roshdy, "Research on the mechanical design of two-axis fast steering mirror for optical beam guidance," *Proceedings of 2012 International Conference on Mechanical Engineering and Material Science (MEMS 2012)*, 2012.
- [5] M. Hafez, T. Sidler, R. Salathe, G. Jansen, and J. Compter, "Design and simulations and experimental and investigations of a compact single mirror tip/tilt laser scanner," *Mechatronics*, vol. 10, pp. 741–760, 2000.
- [6] H. Yoo, M. E. van Royen, W. A. van Cappellen, A. B. Houtsmuller, M. Verhaegen, and G. Schitter, "Automated spherical aberration correction in scanning confocal microscopy," *Review of Scientific Instruments*, vol. 85, p. 123706, 2014.
- [7] Q. Zhou, P. Ben-Tzvi, D. Fan, and A. A. Goldenberg, "Design of fast steering mirror and systems for precision and laser beams and steering," *IEEE International Workshop on Robotic and Sensors Environments, Ottawa, CAN*, 2008.
- [8] L. R. Hedding and R. A. Lewis, "Fast steering mirror design and performance for stabilization and single axis scanning," *SPIE Vol. 1304 Acquisition, Tracking and Pointing IV*, pp. 14–24, 1990.
- [9] C. Fang, J. Guo, G. Q. Yang, Z. H. Jiang, X. H. Xu, and T. F. Wang, "Design and performance test of a two-axis fast steering mirror driven by piezoelectric actuators," *Optoelectronics Letters*, vol. 12, no. 5, p. 333, 2016.
- [10] Y.-x. Xia, Q.-l. Bao, and Q.-y. Wu, "Internal model control of a fast steering mirror for electro-optical fine tracking," *Proc. of SPIE*, vol. 7843, 2010.
- [11] A. Berta, L. Hedding, C. Hoffman, and M. Messaros, "Development of a commercial line of high-performance, fast-steering mirrors," *SPIE*, vol. 3787, pp. 181–192, July 1999.
- [12] S. Xiang, S. Chen, X. Wu, D. Xiao, and X. Zheng, "Study on fast linear scanning for a new laser scanner," *Optics & Laser Technology*, vol. 42, no. 1, pp. 42–46, Feb 2010.
- [13] G. Schitter, P. Thurner, and P. Hansma, "Design and input-shaping control of a novel scanner for high-speed atomic force microscopy," *Mechatronics*, vol. 18, no. 5, p. 282, 2008.
- [14] A. J. Flemming and A. G. Wills, "Optimal periodic trajectories for band-limited systems," *IEEE Transactions on Control Systems Technology*, vol. 17, no. 3, p. 552, 2009.
- [15] H. W. Yoo, S. Ito, and G. Schitter, "Iterative learning control of a galvanometer scanner for fast and accurate scanning laser microscopy," *Control Engineering Practice*, vol. 50, pp. 12–21, 2015.
- [16] M. Sweeney, G. Rynkowski, M. Ketabchi, and R. Crowley, "Design considerations for fast steering mirrors (fsm's)," *Optical Scanning 2002, Proceedings of SPIE*, vol. 4773, 2002.
- [17] R. M. Schmidt, G. Schitter, A. Rankers, and J. van Eijk, *The Design of High Performance Mechatronics*, 2nd ed. Delft University Press, 2014.
- [18] T. Tuma, J. Lygeros, V. Kartik, A. Sebastian, and A. Pantazi, "High-speed multiresolution scanning probe microscopy based on lissajous scan trajectories," *Nanotechnology*, vol. 23, no. 18, p. 185501, 2012.

- [19] T. Tuma, J. Lygeros, A. Sebastian, and A. Pantazi, "Optimal scan trajectories for high-speed scanning probe microscopy," *2012 American Control Conference (ACC)*, 2012.
- [20] S. Z. Sullivan, R. D. Muir, J. A. Newman, M. S. Carlsen, S. Sreehari, C. Doerge, N. J. Begue, R. M. Everly, C. A. Bouman, and G. J. Simpson, "High frame-rate multichannel beam-scanning microscopy based on lissajous trajectories," *Optics Express*, vol. 22, no. 20, p. 24224, 2014.
- [21] H. Feng, H. Gu, D. Silberzweig, E. Stern, and Y. Yang, "Single-shot mr imaging using trapezoidal-gradient-based lissajous trajectories," *IEEE Transactions on Medical Imaging*, vol. 22, no. 8, p. 925, 2003.
- [22] A. Bazaie, Y. K. Yong, and S. R. Moheimani, "High-speed lissajous-scan atomic force microscopy: Scan pattern planning and control design issues," *Review of Scientific Instruments*, vol. 83, no. 6, p. 63701, 2012.
- [23] F. Werner, N. Gdaniec, and T. Knopp, "First experimental comparison between the cartesian and the lissajous trajectory for magnetic particle imaging," *Physics in Medicine and Biology*, vol. 62, no. 9, p. 3407, 2017.
- [24] K. Hwang, Y. H. Seo, and K. H. Jeong, "Microscanners for optical endomicroscopic applications," *Micro and Nano Systems Letters*, vol. 5, no. 1, 2017.
- [25] E. Csencsics, R. Saathof, and G. Schitter, "Design of a dual-tone controller for lissajous-based scanning of fast steering mirrors," *2016 American Control Conference, Boston, MA, USA*, submitted 2016.
- [26] J. Morrison, M. Imboden, and D. J. Bishop, "Tuning the resonance frequencies and mode shapes in a large range multi-degree of freedom micromirror," *Optics Express*, vol. 25, no. 7, pp. 7895–7906, 2017.
- [27] S. Skogestad and I. Postlethwaite, *Multivariable Feedback Control*. John Wiley, New York, 2005.
- [28] H. Kwakernaak, "Robust control and hinf-optimization - tutorial paper," *Automatica*, vol. 29, no. 2, p. 255, 1993.
- [29] G. F. Franklin, D. J. Powell, and M. L. Workman, *Digital Control of Dynamic Systems*. Prentice Hall, 1997.



Ernst Csencsics is PhD student at the Automation and Control Institute (ACIN) at Vienna University of Technology. He received a MSc. degree in Electrical Engineering from TU Vienna, Austria (2014).

His primary research interests are on high performance mechatronic systems design, control of opto-mechatronic systems, precision engineering, and in-line metrology systems.



Georg Schitter is Professor at the Automation and Control Institute (ACIN) of the Vienna University of Technology. He received a MSc. in Electrical Engineering from TU Graz, Austria (2000) and his PhD degree from ETH Zurich, Switzerland (2004).

His primary research interests are on high-performance mechatronic systems and multidisciplinary systems integration, particularly for precision engineering applications in the high-tech industry, scientific instrumentation, and mechatronic imaging systems, such as scanning probe microscopy, adaptive optics, and lithography systems for semiconductor industry.